Advanced Materials

ADVANCED MATERIALS
www.advmat.de

RESEARCH ARTICLE

Uniaxial Strain Tuned Magnetism of the Altermagnet Candidate H-FeS

Weiliang Yao[1,2] | Feng Ye[3] | Zachary J. Morgan[3] | Douglas L. Abernathy[3] | Ruixian Liu[4] | Sijie Xu[1,2] | Yuxiang Gao[1,2] | Kevin Allen[1,2] | Yuan Fang[1,2] | Emilia Morosan[1,2] | Qimiao Si[1,2] | Pengcheng Dai[1,2]

[1]Department of Physics and Astronomy, Rice University, Houston, Texas, USA | [2]Rice Laboratory for Emergent Magnetic Materials and Smalley-Curl Institute, Rice University, Houston, Texas, USA | [3]Neutron Scattering Division, Oak Ridge National Laboratory, Oak Ridge, Tennessee, USA | [4]Center for Advanced Quantum Studies and Department of Physics, Beijing Normal University, Beijing, People's Republic of China

Correspondence: Weiliang Yao (wy28@rice.edu) | Pengcheng Dai (pdai@rice.edu)

Received: 22 April 2026 | **Revised:** 23 June 2026 | **Accepted:** 16 July 2026

Keywords: altermagnetism | electrical transport | magnetoelastic coupling | neutron scattering | uniaxial strain

ABSTRACT

Altermagnets are a newly recognized class of magnetic materials characterized by compensated spin configurations while still breaking time-reversal symmetry and exhibiting unconventional transport phenomena. Hexagonal FeS (h-FeS) is a recently identified altermagnet candidate that shows a spontaneous anomalous Hall effect (AHE) accompanied by a tiny net magnetization. Here, we show that both the spontaneous AHE and magnetization can be effectively suppressed by an in-plane compressive strain. Since neutron diffraction measurements show that the applied uniaxial strain only modifies the in-plane domain population but does not affect the in-plane magnetic structure, the major effect of the applied strain is to tune the small *c*-axis ferromagnetic moment. Our results demonstrate a strong correlation between the tiny net magnetization and the spontaneous AHE in h-FeS, and show that uniaxial strain provides an effective knob to tune both properties in this altermagnet candidate for spintronic applications.

1 | Introduction

The identification of altermagnetism [1, 2] expands the classification of magnetic order beyond ferromagnetism and antiferromagnetism, establishing a third fundamental magnetic state since the discovery of antiferromagnetism in the 1930s [3]. Altermagnetism is defined by a distinct symmetry class in which collinear magnetic order breaks time-reversal symmetry while preserving zero net magnetization [1, 2, 4–6]. This symmetry-based perspective has led to the reclassification of a number of previously known antiferromagnetic (AFM) materials as altermagnets [2, 4, 7, 8], thereby stimulating renewed interest in re-examination of many long-studied magnetic materials.

Similar to antiferromagnets, altermagnets possess no macroscopic magnetization, rendering them robust against external magnetic fields [1, 2, 4–6]. At the same time, their electronic band structures exhibit momentum-dependent spin splitting even in the absence of spin–orbit coupling (SOC), enabling spin-polarized currents analogous to those in ferromagnets [1, 2, 4–6]. As a result, altermagnets can host unusual transport phenomena, including a spontaneous anomalous Hall effect (AHE) [9], which originates from an effective magnetic field associated with time-reversal symmetry breaking and alternating spin polarization, rather than from a net magnetization as in a simple ferromagnet.

The spontaneous AHE is one of the key signatures of an altermagnet, its observation requires not only a sufficient density of charge carriers but also an appropriate magnetic structure [9–11]. To date, the spontaneous AHE has been observed in only a handful of materials among the huge number of proposed

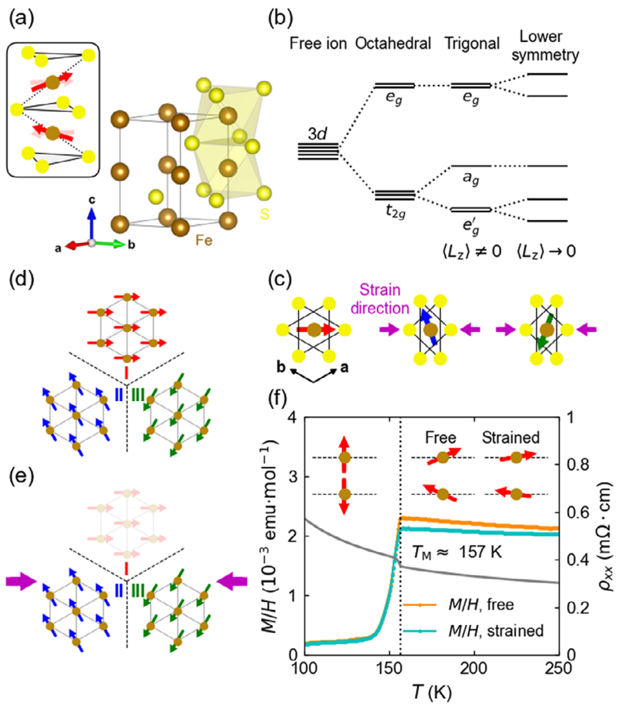

FIGURE 1 | (a) Crystal structure of h-FeS. Two S octahedra surrounding Fe ions are explicitly shown. The upper left inset shows the Fe spin configurations inside the two octahedra, where the spins initially along the $[1\bar{1}0]$ direction exhibit a slight canting toward the Fe-S bonds (dashed lines). (b) Evolution of the orbital states for $3d$ electrons under octahedral, trigonal, and lower-symmetry crystal fields. (c) Top view of the preferred spin directions in the FeS_6 octahedron in the free state and under compressive strain along the $[1\bar{1}0]$ direction (magenta arrows). (d) Three magnetic domains (I, II, and III) in one Fe layer, connected by the C_3 symmetry. (e) Two remaining magnetic domains (II and III) under compressive strain along the $[1\bar{1}0]$ direction. (f) Temperature dependence of the magnetic susceptibility M/H (with and without strain, left axis) and the resistivity (right axis). A magnetic field of 1 T was applied along the c-axis for the M/H data. The inset schematically shows a side-view of the spin configurations. Dashed vertical line marks T_M. The canting angles are intentionally enlarged for better visualization.

altermagnet candidates [12–17]. This scarcity has greatly limited comprehensive studies of altermagnetism-induced spontaneous AHE and its response to external tuning parameters. In addition, the relationship between the spontaneous AHE and the detailed magnetic structures, such as spin canting, remains elusive.

The hexagonal phase of FeS (h-FeS) has recently been identified as an altermagnet candidate showing an intriguing spontaneous AHE [18]. Due to the slight Fe deficiency, the exact crystal structure of h-FeS at a specific temperature depends on the stoichiometry of Fe and S [18–21]. For our samples, the actual chemical composition is close to $Fe_{0.93}S$ [22]. At room temperature, these samples exhibit a NiAs-type structure (space group $P6_3/mmc$) (Figure 1a) [22], where the Fe ions form a triangular lattice in the ab-plane. Similar to the g-wave altermagnets α-MnTe [23, 24] and CrSb [25, 26], the altermagnetism of h-FeS originates from the alternating arrangement of the S octahedra surrounding the Fe ions (Figure 1a). Such structure preserves an overall six-fold rotational (C_6) symmetry even though each individual FeS_6 octahedron possesses only a local threefold rotational (C_3) symmetry. Under the octahedral crystal field, the Fe^{2+} ions adopt a high-spin electronic configuration $t_{2g}^4 e_g^2$ [27, 28], with the orbital states further split by the trigonal and lower-symmetry crystal fields (Figure 1b).

Below $T_N \approx 600$ K, the localized Fe moments develop a long-range magnetic order, aligning predominantly parallel within the ab-plane and antiparallel between adjacent triangular layers (Figure 1a) [19–21, 28]. This so-called A-type AFM structure is further perturbed by additional local magnetocrystalline anisotropy, which induces a small spin canting and gives rise to a tiny net magnetization along the c-axis on the order of 10^{-3} μ_B/Fe [18]. Owing to the lattice's C_6 symmetry, three equivalent in-plane magnetic domains are present (domains I, II, and III in Figure 1d). The spontaneous AHE was observed in this easy-plane spin configuration, which is consistent with symmetry analysis and regarded as direct evidence of the underlying altermagnetism [18]. At lower temperatures, the Fe moments reorient along the c-axis through a Morin transition [19–21, 28, 29], where the spontaneous AHE is symmetry-forbidden. Although the Morin transition temperature (T_M) depends on the Fe and S stoichiometry, the main magnetic structures above and below it are insensitive to the precise value of T_M [19–21, 28–30].

Strain has been widely thought to be an effective tool for controlling altermagnetism, ranging from modifying electronic band structures [31–35] to tuning spin configurations [36–38]. In this work, we explore the impact of uniaxial strain on the magnetic properties of h-FeS. We find that both the spontaneous AHE and the small net magnetization are simultaneously suppressed by compressive strain applied within the ab-plane. Neutron diffraction measurements under similar in-plane uniaxial strain further show that while the overall magnetic structure remains unchanged, the reduction of the AHE and magnetization is accompanied by a repopulation of in-plane magnetic domains. Such facile tunability of magnetic domains is consistent with a vanishingly small spin-wave gap, as directly revealed by inelastic neutron scattering (INS). These results demonstrate that the strain-reduced spontaneous AHE in h-FeS is correlated with suppressed spin canting, both of which are rooted in SOC and associated magnetoelastic coupling.

2 | Results and Discussion

Figure 1f shows the magnetic susceptibility measured at 1 T as a function of temperature, which exhibits a sudden drop below T_M. This behavior indicates a transition of the magnetic structure from an easy-plane spin configuration at high temperatures to an easy-axis spin configuration at low temperatures (see the inset of Figure 1f). Consistent with this magnetic transition, the temperature dependence of the in-plane resistivity displays a clear kink at T_M, reflecting the influence of the magnetic structure change on electrical transport. These characterization results are qualitatively consistent with previous reports [18–20], although the exact value of T_M depends on the chemical composition.

Figure 2a–d presents the in-plane Hall resistivity under c-axis fields at selected four temperatures. At 140 K, which is below $T_M \approx 156$ K for this sample, the Hall resistivity varies linearly

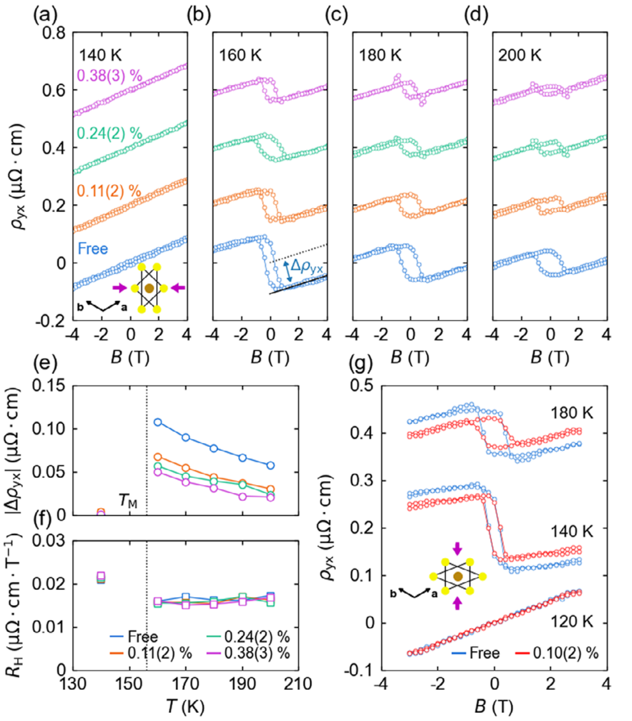

FIGURE 2 | (a–d) Magnetic-field dependence of the Hall resistivity measured at selected temperatures under compressive strain applied along [1$\bar{1}$0]. Magnetic fields are applied along the *c*-axis. The solid line in (b) represents a linear fit to the data, as described in the text. For clarity, the data are vertically offset by 0.2 $\mu\Omega \cdot$cm. (e) and (f) Temperature dependence of the fitted anomalous Hall resistivity and the *B*-linear Hall coefficient at different strain magnitudes. (g) Magnetic-field dependence of the Hall resistivity measured at selected temperatures under compressive strain applied along [110]. Insets in (a) and (g) illustrate the corresponding strain directions.

with magnetic field, indicating that the response is dominated by the ordinary Hall effect (proportional to the magnetic field) and the conventional AHE (proportional to the magnetization). A spontaneous AHE emerges above T_M when the spins lie in the *ab*-plane, and its magnitude decreases with increasing temperature. Upon applying a compressive strain along [1$\bar{1}$0] direction [39], the spontaneous AHE is gradually suppressed (Figure 2b–d), while the contributions from ordinary Hall effect and conventional AHE are basically unchanged.

To quantitatively determine the spontaneous AHE, we fit the high-field region ($B > 2$ T) of the Hall resistivity using the phenomenological expression $\rho_{yx}(B) = R_H B + \Delta\rho_{yx}$, where the first term represents the *B*-linear contribution from the ordinary Hall effect and the conventional AHE (excluding the spontaneous part), and the second term corresponds to the spontaneous AHE. A representative fit for the data at 160 K without applied strain is shown in Figure 2b. The temperature dependencies of the fitting parameters (R_H and ρ_{yx}) under various strain conditions are summarized in Figure 2e,f, respectively. Assuming $\Delta\rho_{yx}$ is a signature of altermagnetism in h-FeS [18], its systematic suppression suggests that altermagnetism can be effectively tuned by an in-plane strain. In contrast, the strain dependence of R_H (Figure 2f) suggests that the overall electronic band structure is not dramatically affected by the size of the applied strain. We

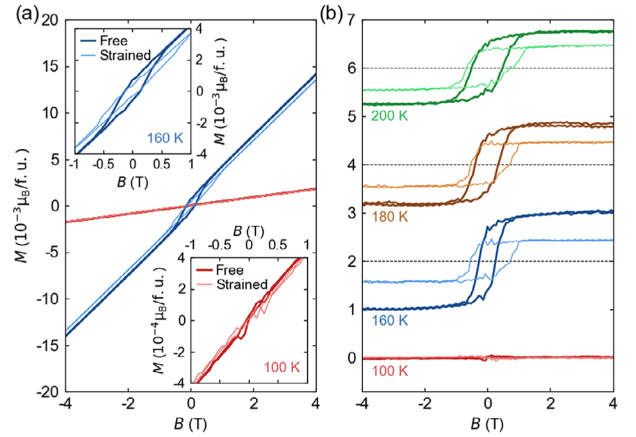

FIGURE 3 | (a) Isothermal magnetization along the *c*-axis with and without compressive strain applied along [1$\bar{1}$0] at 100 K (< T_M) and 160 K (> T_M). Insets show the zoom-in view of data within ± 1 T. (b) Isothermal magnetization along the *c*-axis at selected temperatures after subtracting the high-field linear part. Light and dark colors denote data with and without strain, respectively. Data are evenly offset 0.002 μ_B/f.u. for clarity.

further note that the spontaneous AHE is similarly suppressed by compressive strain applied along [110] direction (perpendicular to [1$\bar{1}$0]), as shown in Figure 2g.

Having established the strain-tuned spontaneous AHE, we next investigate the effect of uniaxial strain on the magnetization. Figure 3a shows the isothermal magnetization measured along the *c*-axis direction. Below T_M, the magnetization arises solely from the AFM structure and thus exhibits a linear dependence on the applied magnetic field. When spin canting develops above T_M, a small hysteresis loop emerges in the low-field region, indicating a weak ferromagnetic contribution, although the overall magnetization remains predominantly linear with respect to the field. Therefore, above T_M, the magnetization consists of both an AFM component and a ferromagnetic component. With the application of a compressive strain along [1$\bar{1}$0] direction, the small ferromagnetic component that appears only above T_M is reduced (Figure 3a). However, the differential AFM susceptibility (i.e., the slope of the linear background) is not affected both above and below T_M. This behavior is further corroborated by the temperature dependence of the magnetic susceptibility shown in Figure 1f, where M/H is reduced by strain above T_M, but remains nearly unchanged below T_M. To isolate the strain effect, we present the magnetization data after subtracting the AFM contribution, as shown in Figure 3b. It can be more clearly seen that the magnitude of the ferromagnetic component is suppressed under strain.

Since the ferromagnetic component originates from spin canting [18], these results indicate that compressive strain applied within the Fe triangular plane (Figure 1d,e) effectively suppresses the *c*-axis spin canting in h-FeS. On the same sample used for these magnetization measurements, we have independently confirmed the strain-suppressed spontaneous AHE [22]. Although the small ferromagnetic component is believed to be noncritical for the spontaneous AHE [18], the concurrent suppression of both the AHE and the ferromagnetic moment under in-plane uniaxial strain suggests a close correlation between the two phenomena in

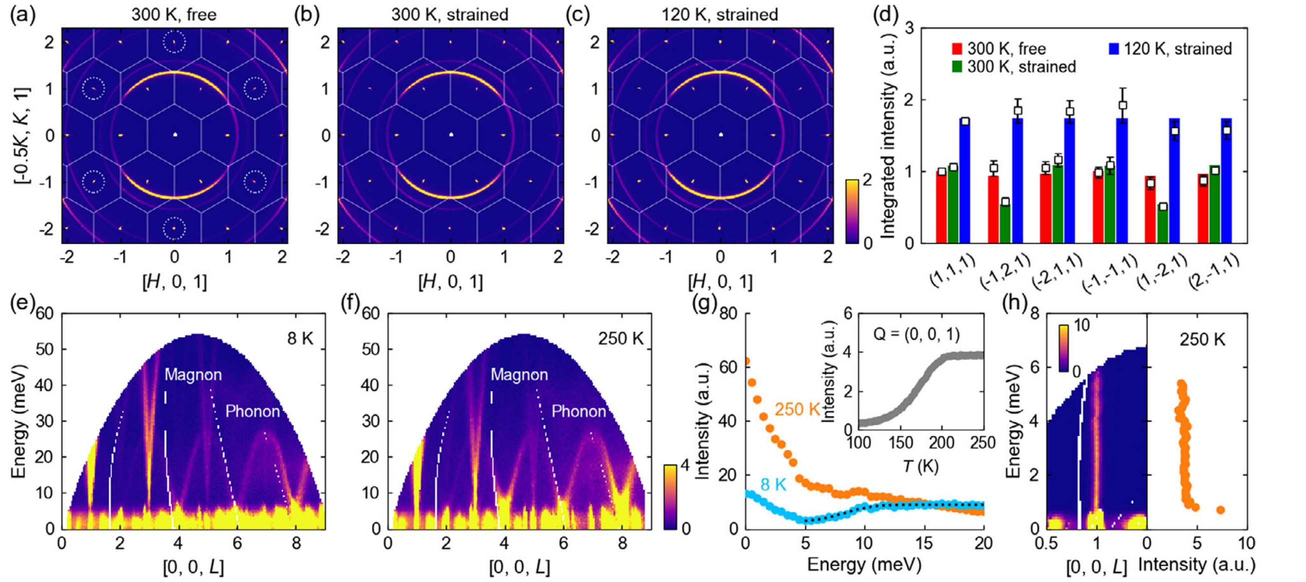

FIGURE 4 | (a–c) Neutron diffraction patterns in the $(H, K, 1)$ plane measured at 300 K without strain, 300 K with strain, and 120 K with strain, respectively. White hexagons indicate the Brillouin zone boundaries. Dashed circles in (a) mark the Bragg peaks whose integrated intensities are shown in (d). Compressive strain is applied along the horizontal axis in (b) and (c). (d) Integrated intensities (square symbols with error bars) of six Bragg peaks under the three conditions. The bar chart represents the corresponding calculated intensities [22]. (e) and (f) INS spectra measured along the $[0, 0, L]$ direction at 8 K and 250 K, respectively. (g) Energy dependence of the excitation intensity at (0, 0, 1) measured at 8 K and 250 K. The dashed curve shows a fit to the spin-wave gap using an error function [22]. The inset displays the temperature dependence of the diffraction intensity at the (0, 0, 1) Bragg peak. (h) Left: low-energy excitation spectrum around (0, 0, 1) at 250 K. Right: the corresponding energy dependence of the intensity at (0, 0, 1).

h-FeS. On the other hand, the field-induced AFM magnetization does not contribute to the spontaneous AHE. Based on the level of strain we applied, estimated to be 0.25(2)%, we determine the piezomagnetic coefficient of h-FeS to be $\sim 10^{-3}$ G $\cdot$ MPa^{-1} at 160 K. This value is about one order of magnitude smaller than in Mn_3Sn [40], yet three orders of magnitude larger than in α-MnTe [36], both of which, interestingly, also exhibit strain-tuned spontaneous AHEs [40–42]. We note that, because the temperatures, field orientations, and strain levels differ among these studies, the comparison here is only meant to show the order of magnitude.

To gain further insight into the effects of in-plane compressive strain, we performed neutron diffraction measurements on h-FeS single crystals. Figure 4a–c shows neutron diffraction patterns in the $(H, K, 1)$ plane under three conditions: 300 K without applied strain, 300 K with compressive strain along the $[1\bar{1}0]$ direction (above T_M), and 120 K with compressive strain along the same direction (below T_M). Although all Bragg peaks remain at integer-index positions, the intensities of some peaks exhibit pronounced changes. Figure 4d shows the integrated intensities of the (1, 1, 1) Bragg peak and its five symmetry-equivalent counterparts in the unstrained case (Figure 4a). Because the nuclear structure factor vanishes at these reflections, their intensities can be attributed solely to the magnetic scattering. At 300 K without strain, the six peaks show nearly identical intensities. However, when the strain is applied, the intensities of (−1, 2, 1) and (1, −2, 1) peaks are significantly reduced, whereas those of the remaining four peaks increase slightly. Such behavior can be well accounted for by strain-induced redistribution of in-plane magnetic domains above T_M [22], and closely resembles that observed in α-MnTe [41], which hosts the same A-type AFM structure. In the absence of strain, the three magnetic domains are equally populated (Figure 1d). Upon applying strain, however, the magnetic domain whose spins are aligned along the strain direction (i.e., domain I in Figure 1d) is strongly suppressed, leaving only the other two domains with dominant populations (Figure 1e).

From the measured integrated intensities, we estimate that the population ratio of domain I:domain II:domain III is 0.31(4):0.33(4):0.36(4) in the absence of strain, and changes to 0.02(4):0.49(3):0.49(3) under applied strain [22]. Below T_M, the intensities of the six peaks become comparable again even in the presence of strain (Figure 4d), consistent with the easy-axis spin configuration. This behavior further confirms that the observed intensity variations originate from the magnetic response to strain, rather than from changes in the lattice itself. We point out that the intensity change due to strain-induced spin canting is on the order of 10^{-7} [22], as estimated from the c-axis ferromagnetic moment in the magnetization measurements (Figure 3), and therefore lies well below the sensitivity of the unpolarized neutron diffraction technique used here. Moreover, such in-plane strain-driven domain repopulation is not expected to affect the strength of the spontaneous AHE, which behaves as an axial vector oriented along the c-axis. A detailed symmetry analysis of the conductivity tensor under strain is provided in [22].

The ease with which magnetic domains can be tuned by strain is also manifested in the spin excitations. Figure 4e and Figure 4f present the INS-measured excitation spectra along the $[0, 0, L]$ direction below and above T_M, respectively, where dispersive spin waves emanating from $L = 1$ and 3 are observed. From the energy dependence of the intensity at (0, 0, 1) (Figure 4g), we find that the spin-wave gap of 8.3(3) meV at 8 K is filled in at 250 K, accompanied by an accumulation of elastic magnetic scattering intensity at (0, 0, 1) (inset of Figure 4g). With improved energy resolution, the spin-wave gap above T_M is found to be smaller than 0.5 meV, as shown in Figure 4g, which corresponds to the energy resolution at zero energy transfer [22]. The strongly reduced gap indicates that spins can more readily overcome the energy barrier separating the three magnetic domains in the easy-plane spin configuration. Consequently, the application of stress, even on the order of 100 MPa, is sufficient to lift the energy degeneracy among the three in-plane spin directions and selectively stabilize two domains. This situation is very similar to spin-wave gaps in pure and Li-doped α-MnTe, where Li-doping into pure α-MnTe induces a large spin anisotropy gap of ∼6 meV and rotates the moment from the in-plane to the c-axis direction [43–46].

Finally, we discuss the origin of the strain-tuned spin canting in terms of subtle strain-induced changes in the local coordination of the Fe ions. They are closely tied to magnetocrystalline anisotropy of h-FeS, which has been extensively studied for over six decades [19, 47–50]. We first note that the orientation of the Fe magnetic moments is collectively determined by the crystal field, exchange interactions, and SOC, all of which depend sensitively on the lattice parameters a and c within the NiAs-type structure [19, 47–50]. At high temperatures, where the ratio c/a is smaller than a critical value, the crystal field and exchange interactions together favor an easy-plane anisotropy, while the SOC promotes an out-of-plane spin canting [19, 47, 51, 52]. Since the former two interactions are much stronger than the SOC, the spins exhibit only a small canting angle while remaining predominantly in plane. When an in-plane uniaxial strain is applied, the local C_3 symmetry of the FeS_6 octahedron is broken (Figure 1c). The partially quenched orbital angular momentum is further reduced, thereby lifting the remaining orbital degeneracy [53, 54] (Figure 1b). This additional quenching of the orbital angular momentum naturally weakens the effectiveness of SOC [51, 52, 55, 56], leading to a reduction of the spin canting and, consequently, a suppression of the spontaneous AHE. A more detailed analysis is provided in [22]. This behavior re-manifests the famous Jahn–Teller effect, where the lattice distortion spontaneously occurs accompanied by quenching of the orbital angular momentum [57]. Since the spontaneous AHE and the accompanying weak ferromagnetism are consistently observed in the easy-plane spin configuration above T_M, irrespective of its exact value, the strain-induced symmetry-lowering mechanism is expected to operate generally in h-FeS across a wide range of Fe deficiencies. We note that the established magnetocrystalline anisotropy theory has also successfully explained both the Mori transition at T_M and the reduction of spin canting with increasing temperature (Figure 3) [47–50]. This framework is again consistent with the experimentally observed suppression of the spontaneous AHE at elevated temperatures (Figure 2) [18].

The direct correlation between the spontaneous AHE and the weak ferromagnetic moment indicates that these two responses are not independent in h-FeS. This provides an experimental perspective complementary to the work by Takagi et al., which argues that the spontaneous AHE does not require tiny spin canting (or ferromagnetic moment) and can originate from the symmetry-allowed Berry curvature of the collinear AFM order alone [18]. In the present work, both the spontaneous AHE and the weak ferromagnetic moment are suppressed by uniaxial strain and exhibit closely related temperature dependences, suggesting that their connection is unlikely to be accidental. In conventional ferromagnets, the spontaneous anomalous Hall resistivity (ρ^A) is proportional to the net magnetization (M), $\rho^A = R_S \mu_0 M$, where R_S is the anomalous Hall coefficient and μ_0 is the vacuum permeability [58]. From this phenomenological viewpoint, h-FeS behaves like a weak ferromagnet with a small net magnetization but an exceptionally large $|R_S|$ (on the order of 100 $\mu\Omega \cdot cm \cdot T^{-1}$), far exceeding the values in typical ferromagnets. For comparison, $|R_S|$ is below 1 $\mu\Omega \cdot cm \cdot T^{-1}$ in elemental Fe and Ni [59, 60]. Our findings do not necessarily require abandoning the Berry-curvature explanation. Rather, they suggest that the weak ferromagnetic moment and the spontaneous AHE are intrinsically linked and likely controlled by the same underlying symmetry condition. Further theoretical investigations are required to clarify the microscopic origin of the unusually large anomalous Hall coefficient in h-FeS and its relation to the weak ferromagnetic moment.

Notably, h-FeS belongs to a broader class of compensated magnets exhibiting large spontaneous AHEs, which include α-MnTe [12–14, 16, 17], Mn_3A (A = Sn, Ge, and Pt) [61–63], Ce_2BGe_6 (B = Cu and Pd) [64], and CoC_3S_6 (C = Nb and Ta) [65–67]. Their spontaneous AHEs have been attributed either to nontrivial band structure effect (Berry curvature) in reciprocal space, or real space non-coplanar spins and associated nonzero scalar spin chirality. Nevertheless, all of these materials exhibit a small but detectable net magnetization concomitant with the AHE. While this magnetization is generally considered too small to account for the large spontaneous AHE, it would be interesting to experimentally examine whether simultaneous tuning of the magnetization and the spontaneous AHE, as established in h-FeS, can also be achieved in these materials.

3 | Conclusion

In summary, by combining electrical transport, magnetization, and neutron scattering measurements, we have systematically studied the magnetism of the altermagnet candidate h-FeS under in-plane compressive strain. We find that both the spontaneous AHE and the small ferromagnetic moment are suppressed by a uniaxial strain, which can be understood in terms of strain-induced tuning of the local coordination environment of the magnetic Fe ions. Neutron diffraction further reveals that, while the dominant magnetic structure remains unchanged, strain redistributes the magnetic domains of the easy-plane spin configuration, consistent with the negligible spin-wave gap observed by INS. Our results demonstrate that the spontaneous AHE in h-FeS, a hallmark of altermagnetism, is closely correlated with the weak ferromagnetic moment arising from spin canting, and establish uniaxial strain as an effective control parameter for tuning magnetism in altermagnet candidates.

4 | Experimental Section

4.1 | Single Crystal Growth Method

Single crystals of h-FeS were grown using a chemical vapor transport method, slightly modified from previous reports

[28, 68–71]. A mixture of 3.81 g iron powder, 2.28 g sulfur powder, and 0.22 g iodine was loaded into a quartz tube (outer diameter 28 mm, wall thickness 1.5 mm), which was then evacuated and sealed under vacuum. The sealed portion of the tube was approximately 23 cm in length. The tube was placed in a tube furnace, where the temperatures of the hot and cold ends were independently and sequentially controlled. The starting materials were positioned at the hot end of the tube. The hot and cold ends were heated to 940°C and 840°C, respectively, over 10 h and maintained at these temperatures for 240 h. Afterward, the furnace was turned off and allowed to cool naturally to room temperature. Single crystals with hexagonal edges were obtained at the cold end of the tube. We find that using fine Fe powder is advantageous for growing larger crystals, although the physical properties of the obtained samples remain the same. The growth duration of 240 h was selected based on our experience and optimized growth conditions, which reliably produce relatively large h-FeS single crystals. A shorter growth duration generally produces smaller crystals. Although extending the growth time can increase the overall crystal size, we find that the crystals may overlap or stack because of the limited space at the cold end of the quartz tube. This can lead to intergrown crystals containing multiple structural domains. Such crystals are difficult to separate because h-FeS is relatively hard. Therefore, this growth duration provides an appropriate balance between obtaining large crystals and avoiding excessive intergrowth. Detailed sample characterization results can be found in the Supporting Information, which includes Figures S1–S5 and Tables S1–S3.

4.2 | Electrical Transport Measurements Under Uniaxial Strain

Electrical transport measurements were performed using a Quantum Design PPMS equipped with the electrical transport option. The h-FeS single crystals used in these measurements were cut and polished into approximate thin cuboids prior to making electrical contacts. Uniaxial compressive strain was applied using a small home-made mechanical strain device fabricated from brass (Figure S6a). The magnitude of the applied strain was estimated from the displacement associated with the advancement of the screw in the strain device and the Young's modulus of h-FeS (∼20 GPa), which was determined from the acoustic phonon dispersion (see Figure 4e,f and also [28]). Further details on the estimation of the applied strain are provided in the Supporting Information (see Figure S7 and Tables S4 and S5). The Hall resistivity was extracted from the measured Hall signal by antisymmetrizing the data according to,

$$\rho_{yx}(B) = [\rho(+B) - \rho(-B)]/2 \tag{1}$$

thereby eliminating contributions arising from voltage-probe misalignment. Additional electrical transport data are presented in Figures S8 and S9.

4.3 | Magnetization Measurements Under Uniaxial Strain

Magnetization measurements were also performed using a Quantum Design PPMS equipped with the vibrating sample magnetometer option. Uniaxial compressive strain was applied using the same strain device as that employed in the electrical transport measurements (Figure S6b), ensuring direct comparability between the two types of measurements. The magnitude of the applied strain was estimated using the same method as in the electrical transport experiments. The compressive strain was applied along $[1\bar{1}0]$, and the magnetic field was applied along the *c*-axis. The raw data for the magnetization measurements shown in the main text are provided in Figures S10 and S11. In Figure S12, we present data from another sample to further confirm our results.

4.4 | Neutron Diffraction Under Uniaxial Strain

Neutron diffraction experiments were conducted on the CORELLI diffractometer installed at the Spallation Neutron Source of Oak Ridge National Laboratory [72]. Uniaxial strain was applied using a homemade strain device fabricated from aluminum (Figure S13a) [41]. A piece of h-FeS single crystal with a mass of about 60 mg was used, and the strain was applied along $[1\bar{1}0]$. The magnitude of the applied stress is approximately 100 MPa for the strained state, as estimated from the displacement associated with the advancement of the screw in the strain device and the Young's modulus of h-FeS [41]. Since mechanical strain devices were used in our experiments, the applied strains were controlled by tightening or loosening a screw. Consequently, the strains used in the different measurements, including electrical transport, magnetization, and neutron diffraction, could not be made exactly identical. Nevertheless, all applied strains were within the same order of magnitude (0% ∼ 0.5%). Additional neutron diffraction data are presented in Figures S13–S15.

4.5 | Inelastic Neutron Scattering Measurements

INS experiments were performed on the ARCS spectrometer at the Spallation Neutron Source, Oak Ridge National Laboratory [73]. A coaligned h-FeS single-crystal array with a total mass of ∼19.5 g was used in this experiment (Figure S16a). The $(H, 0, L)$ plane (within the NiAs-type structure) was aligned in the horizontal scattering plane. The overall sample mosaic is approximately 1°, as determined from rocking scans of the structural Bragg peaks (0, 0, 2) and (−1, 0, 0) (Figure S16). Data reduction and analysis were carried out using Mantid [74] and Horace [75]. The incident neutron energies (E_is), chopper frequencies, energy resolutions at zero energy transfer, and momentum integration ranges used for the presented data are summarized in Table S6. Additional INS data about chiral magnon splitting are presented in Figure S17.

Acknowledgements

The single-crystal synthesis, transport, magnetization, and neutron scattering experiments at Rice were supported by the U.S. DOE, BES under Grant Nos. DE-SC0012311 (P.D.) and DE-SC0026179 (P.D., Q.S., and E.M.). Part of the materials characterization efforts at Rice is supported by the Robert A. Welch Foundation Grant No. C-1839 (P.D.). Part of the theoretical efforts at Rice is supported by the Robert A. Welch Foundation Grant No. C-1411 (Q.S.). A portion of this research used resources at the

Spallation Neutron Source, a DOE Office of Science User Facility operated by the Oak Ridge National Laboratory. The beam time was allocated to CORELLI on Proposal No. IPTS-34949.1 and ARCS on Proposal No. IPTS-34948.1.

Conflicts of Interest

The authors declare no conflicts of interest.

Data Availability Statement

Data supporting the findings of this study will be openly available or are available from the corresponding authors upon reasonable request.

References

1. L. Šmejkal, J. Sinova, and T. Jungwirth, "Beyond Conventional Ferromagnetism and Antiferromagnetism: A Phase With Nonrelativistic Spin and Crystal Rotation Symmetry," *Physical Review X* 12 (2022): 031042, https://doi.org/10.1103/PhysRevX.12.031042.

2. L. Šmejkal, J. Sinova, and T. Jungwirth, "Emerging Research Landscape of Altermagnetism," *Physical Review X* 12 (2022): 040501, https://doi.org/10.1103/PhysRevX.12.040501.

3. L. Néel, "Propriétés magnétiques de l'état métallique et énergie d'interaction entre atomes magnétiques," *Annals of Physics* 11, no. 5 (1936): 232–279, https://doi.org/10.1051/anphys/193611050232.

4. L. Bai, W. Feng, S. Liu, L. Šmejkal, Y. Mokrousov, and Y. Yao, "Altermagnetism: Exploring New Frontiers in Magnetism and Spintronics," *Advanced Functional Materials* 34, no. 49 (2024): 2409327, https://doi.org/10.1002/adfm.202409327.

5. C. Song, H. Bai, Z. Zhou, et al., "Altermagnets as a New Class of Functional Materials," *Nature Reviews Materials* 10 (2025): 473–485, https://doi.org/10.1038/s41578-025-00779-1.

6. S. S. Fender, O. Gonzalez, and D. K. Bediako, "Altermagnetism: A Chemical Perspective," *Journal of the American Chemical Society* 147, no. 3 (2025): 2257–2274, https://doi.org/10.1021/jacs.4c14503.

7. X. Chen, Y. Liu, P. Liu, et al., "Unconventional Magnons in Collinear Magnets Dictated by Spin Space Groups," *Nature* 640 (2025): 349–354, https://doi.org/10.1038/s41586-025-08715-7.

8. R. Bhattarai, P. Minch, and T. D. Rhone, "High-Throughput Screening of Altermagnetic Materials," *Physical Review Materials* 9 (2025): 064403, https://doi.org/10.1103/PhysRevMaterials.9.064403.

9. L. Šmejkal, R. González-Hernández, T. Jungwirth, and J. Sinova, "Crystal Time-Reversal Symmetry Breaking and Spontaneous Hall Effect in Collinear Antiferromagnets," *Science Advances* 6, no. 23 (2020): eaaz8809, https://doi.org/10.1126/sciadv.aaz8809.

10. T. Urata, W. Hattori, and H. Ikuta, "High Mobility Charge Transport in a Multicarrier Altermagnet CrSb," *Physical Review Materials* 8 (2024): 084412, https://doi.org/10.1103/PhysRevMaterials.8.084412.

11. T. Yu, I. Shahid, P. Liu, D.-F. Shao, X.-Q. Chen, and Y. Sun, "Néel Vector-Dependent Anomalous Transport in Altermagnetic Metal CrSb," *npj Quantum Materials* 10, no. 1 (2025): 47, https://doi.org/10.1038/s41535-025-00766-3.

12. J. Wasscher, "Evidence of Weak Ferromagnetism in MnTe from Galvanomagnetic Measurements," *Solid State Communications* 3, no. 8 (1965): 169–171, https://www.sciencedirect.com/science/article/pii/003810986590284X.

13. R. D. Gonzalez Betancourt, J. Zubáč, R. Gonzalez-Hernandez, et al., "Spontaneous Anomalous Hall Effect Arising From an Unconventional Compensated Magnetic Phase in a Semiconductor," *Physical Review Letters* 130 (2023): 036702, https://doi.org/10.1103/PhysRevLett.130.036702.

14. K. P. Kluczyk, K. Gas, M. J. Grzybowski, et al., "Coexistence of Anomalous Hall Effect and Weak Magnetization in a Nominally Collinear Antiferromagnet MnTe," *Physical Review B* 110 (2024): 155201, https://doi.org/10.1103/PhysRevB.110.155201.

15. H. Reichlova, R. Lopes Seeger, R. González-Hernández, et al., "Observation of a Spontaneous Anomalous Hall Response in the Mn_5Si_3 d-Wave Altermagnet Candidate," *Nature Communications* 15, no. 1 (2024): 4961, https://doi.org/10.1038/s41467-024-48493-w.

16. L.-J. Zhou, Z.-J. Yan, H. Rong, et al., "Surface-State-Driven Anomalous Hall Effect in altermagnetic MnTe Films," preprint, arXiv, February 10, 2026, arXiv:2602.09363, https://arxiv.org/abs/2602.09363.

17. T.-H. Shao, X. Dai, W. Hu, et al., "Epitaxial Growth and Anomalous Hall Effect in High-Quality Altermagnetic α-MnTe Thin Films," preprint, arXiv, February 12, 2026, arXiv:2602.11645, https://arxiv.org/abs/2602.11645.

18. R. Takagi, R. Hirakida, Y. Settai, et al., "Spontaneous Hall Effect Induced by Collinear Antiferromagnetic Order at Room Temperature," *Nature Materials* 24, no. 1 (2025): 63–68, https://doi.org/10.1038/s41563-024-02058-w.

19. J. Horwood, M. Townsend, and A. Webster, "Magnetic Susceptibility of Single-Crystal $Fe_{1-x}S$," *Journal of Solid State Chemistry* 17, no. 1 (1976): 35–42, https://www.sciencedirect.com/science/article/pii/0022459676901985.

20. J. Coey, H. Roux-Buisson, and R. Brusetti, "Metal-Non Metal Transitions in Transition Metal Compounds. The Electronic Phase Transitions in FeS and NiS," *Le Journal de Physique Colloques* 37, no. C4 (1976): C4, https://doi.org/10.1051/jphyscol:1976401.

21. H. Wang and I. Salveson, "A Review on the Mineral Chemistry of the Non-Stoichiometric Iron Sulphide, $Fe_{1-x}S$ ($0\leq x \leq 0.125$): Polymorphs, Phase Relations and Transitions, Electronic and Magnetic Structures," *Phase Transitions* 78, no. 7–8 (2005): 547–567, https://doi.org/10.1080/01411590500185542.

22. See the Supporting Information for additional data and analyses.

23. S. Lee, S. Lee, S. Jung, et al., "Broken Kramers Degeneracy in Altermagnetic MnTe," *Physical Review Letters* 132 (2024): 036702, https://doi.org/10.1103/PhysRevLett.132.036702.

24. J. Krempaskỳ, L. Šmejkal, S. D'souza, et al., "Altermagnetic Lifting of Kramers Spin Degeneracy," *Nature* 626, no. 7999 (2024): 517–522, https://doi.org/10.1038/s41586-023-06907-7.

25. S. Reimers, L. Odenbreit, L. Šmejkal, et al., "Direct Observation of Altermagnetic Band Splitting in CrSb Thin Films," *Nature Communications* 15, no. 1 (2024): 2116, https://doi.org/10.1038/s41467-024-46476-5.

26. J. Ding, Z. Jiang, X. Chen, et al., "Large Band Splitting in g-Wave Altermagnet CrSb," *Physical Review Letters* 133 (2024): 206401, https://doi.org/10.1103/PhysRevLett.133.206401.

27. S. Sakkopoulos, E. Vitoratos, and T. Argyreas, "Energy-Band Diagram for Pyrrhotite," *Journal of Physics and Chemistry of Solids* 45, no. 8-9 (1984): 923–928, https://doi.org/10.1016/0022-3697(84)90135-5.

28. D. Bansal, J. L. Niedziela, S. Calder, et al., "Magnetically driven Phonon Instability Enables the Metal–Insulator Transition in H-FeS," *Nature Physics* 16, no. 6 (2020): 669–675, https://doi.org/10.1038/s41567-020-0857-1.

29. C. B. V. D. Berg, "Phase Diagram of the Semiconducting Uniaxial Ferroelectric $Fe_{1-X}S$," *Ferroelectrics* 4, no. 1 (1972): 117–120, https://doi.org/10.1080/00150197208235752.

30. A. F. Andresen, P. Torbo, E. Östlund, G. Bloom, and G. Hagen, "Phase Transitions in Fe (X) S (X= 0.90–1.00) Studied by Neutron Diffraction," *Acta Chemica Scandinavica* 21 (1967): 2841–2848.

31. N. Devaraj, A. Bose, and A. Narayan, "Interplay of Altermagnetism and Pressure in Hexagonal and Orthorhombic MnTe," *Physical Review Materials* 8 (2024): 104407, https://doi.org/10.1103/PhysRevMaterials.8.104407.

32. K. D. Belashchenko, "Giant Strain-Induced Spin Splitting Effect in MnTe, a g-Wave Altermagnetic Semiconductor," *Physical Review Letters* 134 (2025): 086701, https://doi.org/10.1103/PhysRevLett.134.086701.

33. K. Takahashi, C. R. W. Steward, M. Ogata, R. M. Fernandes, and J. Schmalian, "Elasto-Hall Conductivity and the Anomalous Hall effect in Altermagnets," *Physical Review B* 111 (2025): 184408, https://doi.org/10.1103/PhysRevB.111.184408.

34. B. Karetta, X. H. Verbeek, R. Jaeschke-Ubiergo, L. Šmejkal, and J. Sinova, "Strain-Controlled g- to d-Wave Transition in Altermagnetic CrSb," *Physical Review B* 112 (2025): 094454, https://doi.org/10.1103/pbbr-hwz4.

35. W. Chen, Z. Zhou, J. Meng, W. Wang, Y. Yang, and Z. Li, "Strain Engineering of Intrinsic Anomalous Hall and Nernst Effects in Altermagnetic MnTe at Realistic Doping Levels," preprint, arXiv, January 06, 2026, arXiv:2601.02913, https://doi.org/10.48550/arXiv.2601.02913.

36. T. Aoyama and K. Ohgushi, "Piezomagnetic Properties in Altermagnetic MnTe," *Physical Review Materials* 8 (2024): L041402, https://doi.org/10.1103/PhysRevMaterials.8.L041402.

37. Z. Zhou, X. Cheng, M. Hu, et al., "Manipulation of the Altermagnetic Order in CrSb Via Crystal Symmetry," *Nature* 638, no. 8051 (2025): 645–650, https://doi.org/10.1038/s41586-024-08436-3.

38. M. Komuro, T. Aoyama, and K. Ohgushi, "Revisiting the Piezomagnetic Effect in the Rutile Fluorides MnF_2 and CoF_2," *Physical Review B* 111 (2025): 214445, https://doi.org/10.1103/t3xl-bxfv.

39. Throughout this work, $[uvw]$ denotes directions in real space, while (H,K,L) and $[H,K,L]$ refer to reciprocal-space coordinates and directions, respectively. Here, the $[1\bar{1}0]$ direction corresponds to the next-nearest-neighbor Fe-Fe bond direction and the [110] direction corresponds to the nearest-neighbor Fe-Fe bond direction in real space.

40. M. Ikhlas, S. Dasgupta, F. Theuss, et al., "Piezomagnetic Switching of the Anomalous Hall Effect in an Antiferromagnet at Room Temperature," *Nature Physics* 18, no. 9 (2022): 1086–1093, https://doi.org/10.1038/s41567-022-01645-5.

41. Z. Liu, S. Xu, J. M. DeStefano, et al., "Strain-Tunable Anomalous Hall Effect in Hexagonal MnTe," *Physical Review X*, https://doi.org/10.1103/589s-s1yy.

42. S. Smolenski, N. Mao, D. Zhang, et al., "Strain-Tunability of the Multipolar Berry Curvature in Altermagnet MnTe," preprint, arXiv, September 25, 2025, arXiv:2509.21481, https://doi.org/10.48550/arXiv.2509.21481.

43. W. Szuszkiewicz, E. Dynowska, B. Witkowska, and B. Hennion, "Spin-Wave Measurements on Hexagonal MnTe of NiAs-Type Structure by Inelastic Neutron Scattering," *Physical Review B* 73 (2006): 104403, https://doi.org/10.1103/PhysRevB.73.104403.

44. Z. Liu, M. Ozeki, S. Asai, S. Itoh, and T. Masuda, "Chiral Split Magnon in Altermagnetic MnTe," *Physical Review Letters* 133 (2024): 156702, https://doi.org/10.1103/PhysRevLett.133.156702.

45. G. Yumnam, D. H. Moseley, J. A. M. Paddison, et al., "Magnon gap Tuning in Lithium-Doped MnTe," *Physical Review B* 109 (2024): 214434, https://doi.org/10.1103/PhysRevB.109.214434.

46. T. Zhang, S. J. G. Alvarado, S. Xu, et al., "Evidence for Itinerant Electron-Local Moment Interaction in Li-Doped α-MnTe," preprint, arXiv, March 18, 2026, arXiv:2512.00747, https://doi.org/10.48550/arXiv.2512.00747.

47. K. Adachi, "Magnetic Anisotropy Energy in Nickel Arsenide Type Crystals," *Journal of the Physical Society of Japan* 16, no. 11 (1961): 2187–2206, https://doi.org/10.1143/JPSJ.16.2187.

48. A. Kengo, "Origine de l'énergie d'anisotropie magnétocristalline de la pyrrhotine," *Journal de Physique France* 24, no. 10 (1963): 725–731, https://doi.org/10.1051/jphys:019630024010072500.

49. K. Sato, "Magnetizing Process of Pyrrhotite Crystal in High Magnetic Field," *Journal of the Physical Society of Japan* 21, no. 4 (1966): 733–737, https://doi.org/10.1143/JPSJ.21.733.

50. K. Adachi and K. Sato, "Origin of Magnetic Anisotropy Energy of Fe_7S_8 and Fe_7Se_8," *Journal of Applied Physics* 39, no. 2 (1968): 1343–1344, https://doi.org/10.1063/1.1656293.

51. L. R. Bickford, "Trigonal Magnetocrystalline Anisotropy in Hexagonal Oxides," *Physical Review* 119 (1960): 1000–1009, https://doi.org/10.1103/PhysRev.119.1000.

52. J. C. Slonczewski, "Origin of Magnetic Anisotropy in Cobalt-Substituted Magnetite," *Physical Review* 110 (1958): 1341–1348, https://doi.org/10.1103/PhysRev.110.1341.

53. P. Fazekas, *Lecture Notes on Electron Correlation and Magnetism*, vol. 5 (World Scientific, 1999).

54. D. I. Khomskii, *Transition Metal Compounds* (Cambridge University Press, 2014).

55. F. S. Ham, "Dynamical Jahn-Teller Effect in Paramagnetic Resonance Spectra: Orbital Reduction Factors and Partial Quenching of Spin-Orbit Interaction," *Physical Review* 138 (1965): A1727–A1740, https://doi.org/10.1103/PhysRev.138.A1727.

56. J. Chappert, A. Misetich, R. B. Frankel, and N. A. Blum, "Stress-Induced Angular Momentum Quenching in MgO: Fe^{2+} as observed by Mössbauer Spectroscopy," *Physical Review B* 1 (1970): 1929–1934, https://doi.org/10.1103/PhysRevB.1.1929.

57. M. C. M. O'Brien and C. C. Chancey, "The Jahn–Teller Effect: An Introduction and Current Review," *American Journal of Physics* 61, no. 8 (1993): 688–697, https://doi.org/10.1119/1.17197.

58. N. Nagaosa, J. Sinova, S. Onoda, A. H. MacDonald, and N. P. Ong, "Anomalous Hall Effect," *Reviews of Modern Physics* 82 (2010): 1539–1592, https://doi.org/10.1103/RevModPhys.82.1539.

59. N. Volkenshtein and G. Fedorov, "Temperature Dependence of the Hall Effect of Pure Ferromagnets," *Soviet Physics—JETP* 11 (1960): 48–50.

60. S. N. Kaul, "Anomalous Hall Effect in Nickel and Nickel-Rich Nickel-Copper Alloys," *Physical Review B* 20 (1979): 5122–5130, https://doi.org/10.1103/PhysRevB.20.5122.

61. S. Nakatsuji, N. Kiyohara, and T. Higo, "Large Anomalous Hall Effect in a Non-Collinear Antiferromagnet at Room Temperature," *Nature* 527, no. 7577 (2015): 212–215, https://doi.org/10.1038/nature15723.

62. A. K. Nayak, J. E. Fischer, Y. Sun, et al., "Large Anomalous Hall Effect Driven by a Nonvanishing Berry Curvature in the Noncolinear Antiferromagnet Mn_3Ge," *Science Advances* 2, no. 4 (2016): e1501870, https://doi.org/10.1126/sciadv.1501870.

63. Z. Liu, H. Chen, J. Wang, et al., "Electrical Switching of the Topological Anomalous Hall Effect in a Non-Collinear Antiferromagnet Above Room Temperature," *Nature Electronics* 1, no. 3 (2018): 172–177, https://doi.org/10.1038/s41928-018-0040-1.

64. H. Kotegawa, H. Tanaka, Y. Takeuchi, et al., "Large Anomalous Hall Conductivity Derived From An f-Electron Collinear Antiferromagnetic Structure," *Physical Review Letters* 133 (2024): 106301, https://doi.org/10.1103/PhysRevLett.133.106301.

65. N. J. Ghimire, A. Botana, J. Jiang, J. Zhang, Y.-S. Chen, and J. Mitchell, "Large Anomalous Hall Effect in the Chiral-Lattice Antiferromagnet $CoNb_3S_6$," *Nature Communications* 9, no. 1 (2018): 3280, https://doi.org/10.1038/s41467-018-05756-7.

66. H. Takagi, R. Takagi, S. Minami, et al., "Spontaneous Topological Hall Effect Induced by Non-Coplanar Antiferromagnetic Order in Intercalated van der Waals Materials," *Nature Physics* 19, no. 7 (2023): 961–968, https://doi.org/10.1038/s41567-023-02017-3.

67. L. Chen, R. Lai, S. Pandey, et al., "Strain-Tunable Anomalous Hall Plateau in Antiferromagnet $CoNb_3S_6$," *Nano Letters* 25, no. 49 (2025): 16970–16976, https://doi.org/10.1021/acs.nanolett.5c03378.

68. G. Krabbes, H. Oppermann, and E. Wolf, "Chemischer Transport von eisensulfid. i. thermodynamische gesichtspunkte beim transport von fesx mit jod – ein beitrag zum problem des transportes von verbindungen mit einem homogenitätsgebiet," *Zeitschrift für anorganische und allgemeine Chemie* 416, no. 1 (1975): 65–82, https://doi.org/10.1002/zaac.19754160109.

69. G. Krabbes, H. Oppermann, and E. Wolf, "Chemischer transport von eisensulfid. ii. experimentelle ergebnisse beim transport von fesx mit jod,"

Zeitschrift für anorganische und allgemeine Chemie 421, no. 2 (1976): 111–121, https://doi.org/10.1002/zaac.19764210204.

70. G. Krabbes, H. Oppermann, and E. Wolf, "Chemischer transport von eisensulfid. iii. der transport von bodenkörpern der zusammensetzung fes1,00," *Zeitschrift für anorganische und allgemeine Chemie* 423, no. 3 (1976): 212–224, https://doi.org/10.1002/zaac.19764230304.

71. M. Binnewies, M. Schmidt, and P. Schmidt, "Chemical Vapor Transport Reactions – Arguments for Choosing a Suitable Transport Agent," *Zeitschrift für anorganische und allgemeine Chemie* 643, no. 21 (2017): 1295–1311, https://doi.org/10.1002/zaac.201700055.

72. F. Ye, Y. Liu, R. Whitfield, R. Osborn, and S. Rosenkranz, "Implementation of Cross Correlation for Energy Discrimination on the Time-of-Flight Spectrometer CORELLI," *Journal of Applied Crystallography* 51, no. 2 (2018): 315–322, https://doi.org/10.1107/S160057671800403X.

73. D. L. Abernathy, M. B. Stone, M. J. Loguillo, et al., "Design and Operation of the Wide Angular-Range Chopper Spectrometer Arcs at the Spallation Neutron Source," *Review of Scientific Instruments* 83, no. 1 (2012): 015114, https://doi.org/10.1063/1.3680104.

74. O. Arnold, J. Bilheux, J. Borreguero, et al., "Mantid-Data Analysis and Visualization Package for Neutron Scattering and μSR Experiments," *Nuclear Instruments and Methods in Physics Research Section A: Accelerators, Spectrometers, Detectors and Associated Equipment* 764 (2014): 156–166, https://www.sciencedirect.com/science/article/pii/S0168900214008729.

75. R. Ewings, A. Buts, M. Le, J. van Duijn, I. Bustinduy, and T. Perring, "Horace: Software for the Analysis of Data From Single Crystal Spectroscopy Experiments at Time-of-Flight Neutron Instruments," *Nuclear Instruments and Methods in Physics Research Section A: Accelerators, Spectrometers, Detectors and Associated Equipment* 834 (2016): 132–142, https://www.sciencedirect.com/science/article/pii/S016890021630777X.

Supporting Information

Additional supporting information can be found online in the Supporting Information section.

Supporting File: adma74398-sup-0001-SuppMat.pdf.